

# Multi-Domain Vibration Diagnosis of Gear Pitting Using a Coupled Torsional-Lateral Spur Gear-Cardan Shaft Model

Yakeu Happi Kemajou Herbert<sup>1</sup>, Bernard Xavier Tchomeni Kouejou<sup>2\*</sup> and Alfayo Anyika Alugongo<sup>2</sup>

<sup>1</sup>Department of Industrial Engineering, Operation Management and Mechanical Engineering, Vaal University of Technology, Andries Potgieter Blvd, 1900 | Private Bag X021, Vanderbijlpark, 1911, South Africa.

<sup>2</sup>Department of Industrial Engineering, Operation Management and Mechanical Engineering, Vaal University of Technology, Andries Potgieter Blvd, 1900 | Private Bag X021, Vanderbijlpark, 1911, South Africa.

**Abstract.** This study proposes an in-depth investigation of pitting failures in a complex mechanical transmission system, based on vibration analysis. This system incorporates a spur gear and a Cardan shaft that shows an angular misalignment. A torsionally-laterally coupled dynamic model of 13 degrees of freedom (DOF) is developed using the Lagrangian formulation. This approach accurately represents the dynamic interactions between mesh excitations and kinematic fluctuations induced by the universal joint. The model explicitly incorporates the progressive degradation of mesh stiffness caused by pit distribution on the tooth surface. The dynamic response of the system is numerically simulated under healthy and then defective operating conditions (pitting affecting 25% of the tooth surface). Multi-domain diagnostic analysis is then performed. This method employs time-domain waveform analysis, Fourier transform (FFT) spectral analysis, time-frequency representations (spectrograms), and visualization of lateral displacement orbits. The results clearly highlight the signature of pitting defects: increased vibration amplitude and amplitude modulation in the time-domain signal, the appearance of characteristic sidebands in the frequency spectrum, and a diffuse structure with energy scattered in the time-frequency plane. Crucially, the combined analysis of lateral and torsional responses demonstrates the effective transmission of defect-generated excitations from the gear subsystem to the Cardan shaft subsystem.

## 1 Introduction

Mechanical power transmission systems are essential components in a wide variety of industrial applications, such as automobile engines, railway systems, rotary machinery, and power conversion equipment. Their role is to reliably transmit torque and motion under varying operating conditions, often characterized by geometric constraints, load fluctuations, and unavoidable misalignments. Among the most common configurations are drive systems that combine spur gear drives with shafts equipped with universal joints (cardan joints). These joints allow torque transmission between misaligned shafts while ensuring mechanical continuity. Despite their robustness, these systems are particularly susceptible to vibration-induced failures due to their inherent dynamic complexity. Spur gears, in particular, are prone to surface degradation phenomena such as pitting, resulting from contact fatigue and the progressive removal of material from the tooth surface. Pitting alters local contact conditions, induces a temporal variation in mesh stiffness, and generates impulsive excitation forces during engagement [1-3]. These effects significantly alter the dynamic response of the drive system and can lead to noise, reduced efficiency, or even catastrophic failure if undetected. At the same time, universal joints show nonhomokinetic behavior when operated with angular

misalignment [4]. This feature produces periodic fluctuations in angular velocity and torque, which interact with the mesh excitations and amplify the complexity of the system dynamics. Therefore, the dynamic coupling between spur gears and universal joints plays a crucial role in transmitting vibrations and fault signatures throughout the transmission. However, many existing studies deal with gear dynamics and universal joint dynamics separately, thus neglecting the strong interaction between these subsystems [5].

Condition monitoring based on vibration analysis has proven to be one of the most effective techniques for early detection of faults in rotating machinery. Time-domain, frequency-domain, and time-frequency analyzes are widely used to identify characteristic signatures associated with gear failures such as pitting, cracking, and tooth breakage. However, the accurate interpretation of these signatures requires physically representative dynamic models capable of accounting for both torsional and lateral vibration modes, as well as failure-induced stiffness variations [6].

To address these limitations, this paper proposes a 13-degree-of-freedom torsionally-laterally coupled dynamic model for a mechanical drive system composed of a spur gear drive and a misaligned Cardan shaft. The model is developed using the Lagrangian formulation and

\* Corresponding author: [bernardt@vut.ac.za](mailto:bernardt@vut.ac.za)

explicitly incorporates the progressive stiffness degradation of the mesh caused by pitting defects distributed on the tooth surface. This coupled model allows us to study how the defect-generated excitations originate in the mesh and propagate through the Cardan shaft subsystem.

Numerical simulations are carried out for both healthy and defective operating conditions, considering a moderate level of pitting severity. The dynamic response is analysed using time-domain waveforms, frequency spectra obtained by fast Fourier transform (FFT), time-frequency plots, and orbital plots of lateral displacements. The results demonstrate that pitting defects produce clear vibration signatures, including amplitude modulation, lateral band shaping, spectral energy dispersion, and orbital deformation. Furthermore, the study highlights the strong transmission of failure-related vibrations from the spur gear to the Cardan shaft, thus confirming the importance of coupled modeling for accurate failure diagnosis.

The paper is organised as follows. Section 2 presents the system description and modeling assumptions. Section 3 introduces the coupled dynamic formulation. Section 4 describes fault modeling and numerical methods. Section 5 discusses the simulation results. Section 6 concludes the study.

## 2. Vibration Analysis of Mechanical Drive System

The system under study is a rotary mechanical drive system consisting of a motor driving a spur gear stage, connected to a drive shaft equipped with a universal joint (Cardan joint), and connected to a resistive load. The motor provides a nominally constant input torque, possibly affected by time fluctuations, and drives the input shaft of the system. This shaft is connected to a spur gear, which is engaged with a gear mounted on an intermediate shaft. The contact between the gear and the gear generates normal and tangential meshing forces, the magnitude of which depends on the stiffness of the mesh and the transmission error. The intermediate shaft is connected to an output shaft via a Cardan-type universal joint. This joint allows the transmission of torque between two shafts forming a misalignment angle, while introducing kinematic nonhomokineticity characterised by a periodic variation in the output angular velocity. The output shaft is finally connected to a mechanical load, modeled by an equivalent inertia and a resistance torque that can be constant and variable depending on the operating conditions.

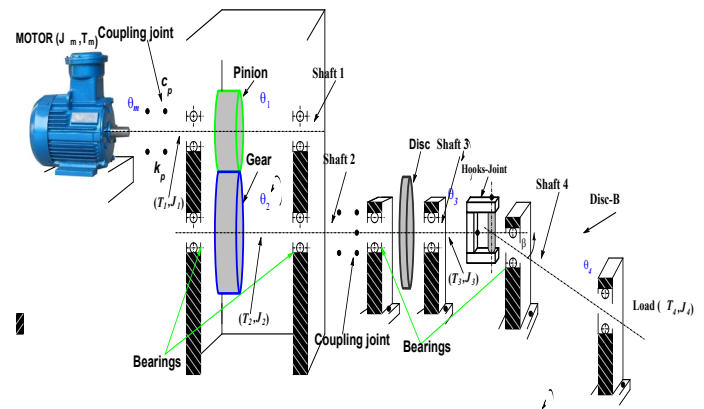


**Fig.1.** Schematic of mechanical drive system formed of a spur gear coupled to a misaligned Cardan shaft.

A dynamic model was developed based on Lagrange's equations in an inertial coordinate system. The following section provides more detailed information about the consideration of the impact of the pitting failure from the spur gear system into the mechanical drive system.

## 3 Introduction of Coupled Dynamic Formulation.

### 3.1. Distribution of Pitting along Tooth Surface

Figure 2 illustrates the uniform distribution of pitting along the tooth length direction.

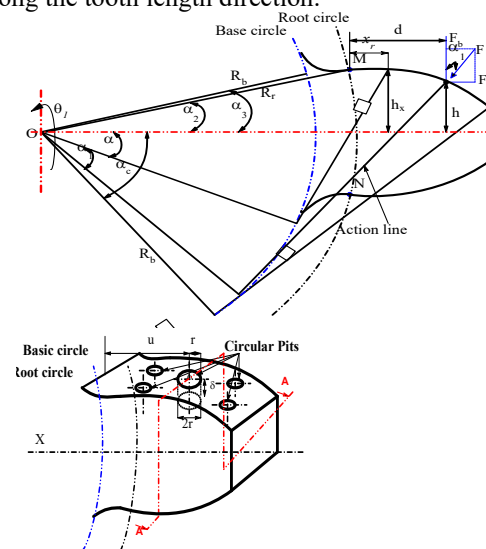


**Fig.2.** Area of the tooth affected by pitting.

### 3.2. Calculation of mesh stiffness for gears with defective teeth

The potential energy method is used to determine the influence of a gear tooth on the overall stiffness. As illustrated in Figure 2, a pinion tooth is modeled as a nonuniform cantilever beam extending from the root circle. The effective contact length  $L$  is not fixed; it decreases when the gear tooth surface has extensive depression during mixing with adjacent teeth. Its expression then becomes  $(L - \Delta L_x)$ , which also modifies the expressions for  $h_x$  (height),  $I_x$  (second moment of

inertia), and  $A_x$  (cross-sectional area), all of which are different from those of a healthy tooth. The terms  $\Delta L_x$ ,  $\Delta A_x$ , and  $\Delta I_x$  describe the reduction in contact length, cross-sectional area, and surface moment of inertia, respectively, where  $x$  represents the distance to the tooth root. Their expressions are calculated as follows:

$$\Delta L_x = \begin{cases} 2\sqrt{r^2 - (u-x)^2}, & x \in [u-r, u+r] \\ 0, & \text{others} \end{cases} \quad (1)$$

$$\Delta A_x = \begin{cases} \Delta L_x \delta, & x \in [u-r, u+r] \\ 0, & \text{others} \end{cases} \quad (2)$$

$$\Delta I_x = \begin{cases} \frac{1}{12} \Delta L_x \delta^3 + \frac{(A_x \Delta A_x (h_x - \frac{\delta}{2}))^2}{A_x - \Delta A_x} & x \in [u-r, u+r] \\ 0 & \text{others} \end{cases} \quad (3)$$

where  $u$  denotes the distance between the tooth root and the center of the circular defect,  $r$  corresponds to the radius of the pit zone, and  $\delta$  represents the depth of the defect. Then, for a gear with a circular defect on the tooth, the Hertzian contact stiffness  $k_h$ , bending stiffness  $k_b$ , axial stiffness  $k_a$ , shear stiffness  $k_s$ , and Hertzian contact stiffness are determined as follows: [7-8]:

$$k_h = \frac{\pi E (L - \Delta L_x)}{4(1 - \mu)} \quad (4)$$

$$\frac{1}{k_{b(\text{pitting})}} = \frac{\left[ 1 - \frac{(Z-2.5)(\cos \alpha_1 \cos \alpha_2)}{Z \cos \alpha_0} \right]^3 - (1 - \cos \alpha_1 \cos \alpha_2)^3}{2EL \cos \alpha_1 + \sin^3 \alpha} + \int_{-\alpha_1}^{\alpha_2} \frac{3 \left[ 1 + \cos \alpha_1 (-\cos \alpha + (\alpha_2 - \alpha) \sin \alpha) \right]^2 (\alpha_2 - \alpha) \cos \alpha}{E \left[ 2L \left( (\alpha_2 - \alpha) \cos \alpha + \sin \alpha \right)^3 - 3 \frac{\Delta L_x}{R_b} \right]} d\alpha \quad (5)$$

$$\frac{1}{k_{s(\text{Pitting})}} = \frac{1.2(1 + \nu) \cos^2 \alpha_1 \left( \cos \alpha_2 - \frac{Z-2.5}{Z \cos \alpha_0} \cos \alpha_3 \right)}{EL \sin \alpha_2} + \int_{-\alpha_1}^{\alpha_2} \frac{1.2(1 + \nu) \cos^2 \alpha_1 (\alpha_2 + \alpha) \cos \alpha \cos^2 \alpha_1}{E \left[ L \left( (\alpha_2 - \alpha) \cos \alpha + \sin \alpha \right) - \frac{1}{2} \frac{\Delta A_x}{R_b} \right]} d\alpha \quad (6)$$

$$\frac{1}{k_{a(\text{Pitting})}} = \frac{\sin^2 \alpha_1 \left( \cos \alpha_2 - \frac{Z-2.5}{Z \cos \alpha_0} \cos \alpha_3 \right)}{2EL \sin \alpha_2} + \int_{-\alpha_1}^{\alpha_2} \frac{(\alpha_2 + \alpha) \cos \alpha \sin^2 \alpha_1}{E \left[ 2L \left( (\alpha_2 - \alpha) \cos \alpha + \sin \alpha \right) - \frac{\Delta A_x}{R_b} \right]} d\alpha \quad (7)$$

The effective stiffness of the mesh results from the serial combination of the different stiffness components, explicitly integrating the effect of local material removal due to pitting is written as follows [9].

$$k_{i(\text{pit})} = \frac{1}{\frac{1}{k_{h(\text{pit})}} + \underbrace{\frac{1}{k_{b_1}} + \frac{1}{k_{s_1}} + \frac{1}{k_{a_1}}}_{\text{tooth of pinion}} + \underbrace{\frac{1}{k_{b_2(\text{pit})}} + \frac{1}{k_{s_2(\text{pit})}} + \frac{1}{k_{a_2(\text{pit})}}}_{\text{damaged gear tooth}}} \quad (8)$$

Based of the description of Figure 1, the full mathematical formulation of the system dynamics is developed in this section, using the Lagrangian formalism to integrate the torsional and lateral degrees of freedom.

### 3.3. Governing Equation of Mechanical Drive System

The following expressions of a mechanical drive system (spur gear subsystem couple Cardan shaft subsystem) equations incorporate the coupling of two shafts (shaft 3 and shaft 4) through the joint.

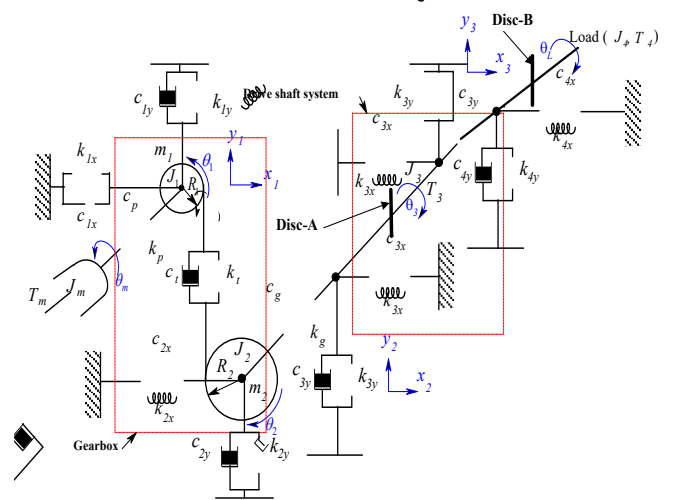


**Fig.3.** Kinematic model of one-stage gearbox dynamics coupled with a Cardan shaft subsystem.

The motion differential equation is calculated by applying the Lagrange equation to different spur gear subsystem and Cardan shaft subsystem components. The dynamic equation of a mechanical drive system with unbalance can be derived from the energy principles and elaborated using the Lagrangian formulation in the inertial coordinate system.

The total kinetic energy of the spur gear subsystem, denoted  $T$ , is formulated as follows based on the geometry of Figure 3:

$$T = \frac{1}{2} m_1 \dot{x}_1^2 + \frac{1}{2} m_2 \dot{x}_2^2 + \frac{1}{2} m_1 \dot{y}_1^2 + \frac{1}{2} m_2 \dot{y}_2^2 + \frac{1}{2} J_1 \dot{\theta}_1^2 + \frac{1}{2} J_2 \dot{\theta}_2^2 + \frac{1}{2} J_m \dot{\theta}_m^2 + \frac{1}{2} J_L \dot{\theta}_L^2 \quad (9)$$

The deformation energy of the gears is integrated into the total potential energy  $U$  of the spur gear subsystem, which is expressed as follows:

$$U = \frac{1}{2}k_1(x_1^2 + y_1^2) + \frac{1}{2}k_2(x_2^2 + y_2^2) + \frac{1}{2}k_p(\theta_m - \theta_1)^2 + \frac{1}{2}k_g(\theta_2 - \theta_L)^2 + \frac{1}{2}k_l[(y_1 + R_1\theta_1) - (y_2 + R_2\theta_2)]^2 \quad (10)$$

The Rayleigh dissipation function  $D$  is formulated as follows, taking into account the viscous damping in the gear system:

$$D = \frac{1}{2}c_1(\dot{x}_1^2 + \dot{y}_1^2) + \frac{1}{2}c_2(\dot{x}_2^2 + \dot{y}_2^2) + \frac{1}{2}c_p(\dot{\theta}_m - \dot{\theta}_1)^2 + \frac{1}{2}c_g(\dot{\theta}_2 - \dot{\theta}_L)^2 + \frac{1}{2}c_l[(\dot{y}_1 + R_1\dot{\theta}_1) - (\dot{y}_2 + R_2\dot{\theta}_2)]^2 \quad (11)$$

where, respectively, the driving gear is 1 and the driven gear is 2.

The total kinetic energy of the Cardan shaft subsystem, denoted  $K$ , is formulated as follows based on the geometry of Figure 1:

$$\begin{aligned} K_{3-4} = & \frac{1}{2}(m_A + m_{\mu_1})(\dot{X}_3^2 + \dot{Y}_3^2) + \frac{1}{2}J_A(\dot{\theta}_A + \dot{\omega}_3)^2 + \\ & m_{\mu_1}e_1^2\dot{\theta}_A\dot{\omega}_3 + \frac{1}{2}m_{\mu_1}e_1^2\dot{\omega}_3^2 + \frac{1}{2}m_{\mu_1}e_1^2\dot{\theta}_A^2(1 + \dot{\omega}_3^2)_3 + \\ & m_{\mu_1}\dot{X}_3\dot{\theta}_A \left[ (e_{1_{y_1}} - \omega_3 e_{1_{x_1}}) \sin \theta_A + (e_{1_{x_1}} + \omega_3 e_{1_{y_1}}) \cos \theta_A \right] + \\ & m_{\mu_1}\dot{Y}_3\dot{\omega}_3 (e_{1_{y_1}} \cos \theta_A - e_{1_{x_1}} \sin \theta_A) - \\ & m_{\mu_1}\dot{X}_3\dot{\omega}_3 (e_{1_{x_1}} \sin \theta_A + e_{1_{y_1}} \cos \theta_A) + \\ & m_{\mu_1}\dot{Y}_3\dot{\theta}_A \left[ (e_{1_{x_1}} - \omega_3 e_{1_{y_1}}) \cos \theta_A - (e_{1_{y_1}} + \omega_3 e_{1_{x_1}}) \sin \theta_A \right] + \\ & \frac{1}{2}(m_B + m_{\mu_2})(\dot{X}_4^2 - \dot{Y}_4^2) + \frac{1}{2}J_B(\dot{\theta}_B + \dot{\omega}_4)^2 + \\ & m_{\mu_2}e_2^2\dot{\omega}_4 + \frac{1}{2}m_{\mu_2}e_2^2\dot{\theta}_B\dot{\omega}_4^2 + \frac{1}{2}m_{\mu_2}e_2^2\dot{\theta}_B^2(1 + \dot{\omega}_4^2) + \\ & m_{\mu_2}\dot{X}_4\dot{\theta}_B \left[ (e_{2_{x_4}} \omega_4 + e_{2_{y_4}}) \cos \theta_B + (e_{2_{y_4}} - \omega_4 e_{2_{x_4}}) \sin \theta_B \right] + \\ & m_{\mu_2}\dot{Y}_4\dot{\omega}_4 (e_{2_{x_4}} \cos \theta_B - e_{2_{y_4}} \sin \theta_B) - \\ & m_{\mu_2}\dot{X}_4\dot{\omega}_4 (e_{2_{x_4}} \sin \theta_B + e_{2_{y_4}} \cos \theta_B) + \\ & m_{\mu_2}\dot{Y}_4\dot{\theta}_B \left[ (e_{2_{y_4}} - \omega_4 e_{2_{x_4}}) \cos \theta_B - (\omega_4 e_{2_{x_4}} + e_{2_{y_4}}) \sin \theta_B \right] \end{aligned} \quad (12)$$

The deformation energy of the Cardan shaft subsystem is integrated into the total potential energy  $U$  of the subsystem, is expressed as follows:

$$U = \frac{1}{2} \left[ k_{x_3} X_3^2 + k_{y_3} Y_3^2 + k_{x_4} X_4^2 + k_{y_4} Y_4^2 + k_{T_{3-A}} \omega_3^2 + k_{T_{4-B}} \left( (1 - \mu(\theta_A)) \omega_3 - \omega_4 \right)^2 \right] \quad (13)$$

where,  $k_{x_3}$ ,  $k_{y_3}$  are stiffness of the shaft 3;  $k_{x_4}$ ,  $k_{y_4}$  are stiffness of the shaft 4;  $k_{T_{3-A}}$  is the rotational stiffness of

the shaft 3-disc A and  $k_{T_{3-B}}$  is rotational stiffness of the shaft 4-disc B.

Considering the effect of the damping coefficient and disregarding the influence of any external force and external torque, Rayleigh's dissipation function can be expressed as

$$R = \frac{1}{2} \left[ c_{x_3} \dot{X}_3^2 + c_{y_3} \dot{Y}_3^2 + c_{x_4} \dot{X}_4^2 + c_{y_4} \dot{Y}_4^2 + c_{T_{3-A}} \dot{\omega}_3^2 + c_{T_{4-B}} \left( (\mu(\theta_A) - 1) \dot{\omega}_3 + \dot{\omega}_4 + \dot{\mu}(\theta_A) \dot{\omega}_4 \right)^2 \right] \quad (14)$$

$C_{x_3}$ ,  $C_{y_3}$  and  $C_{x_4}$ ,  $C_{y_4}$  are translational damping coefficients, and  $c_{T_{3-A}}$ ,  $c_{T_{4-B}}$  are rotational damping coefficients for the shaft 3-disc A and shaft 4-disc B.  $\mu$  is a small perturbation parameter that depends on the angles  $\theta_A$ . It is noted that all the stiffness and damping coefficients are associated with the system degrees of freedom.

To represent the coupled dynamics of the overall model, it is essential to formulate the complete governing equation of motion for the gear subsystem associated with the cardan shaft system. These coupled equations are established using the Lagrangian formulation, to modeling the rotating system with multiple degrees of freedom [10]. Using the expressions for kinetic energy, potential energy, and the Rayleigh dissipation function, the Lagrange equations in their overall form are written as follows:

$$\frac{d}{dt} \left( \frac{\partial T}{\partial \dot{q}} \right) + \frac{\partial D}{\partial \dot{q}} + \frac{\partial U}{\partial q} - \frac{\partial T}{\partial q} = F_q \quad (15)$$

$$q = y_1, y_2, \theta_1, \theta_2, \theta_m, X_3, X_4, Y_3, Y_4, \theta_A, \theta_B, \omega_3, \omega_4$$

The governing equations are represented in matrix form, which facilitates efficient numerical analysis and simulation of the system response, including the impact of misalignment-induced forces and moments. After differentiation and assembly, the global 13-DOF model can be written compactly as,

$$\begin{aligned} [M](\ddot{q}) + [C + C_{uj}(\theta_A, \beta)](\dot{q}) + [K_0 + K_{defect}](q) = \\ [F_{ub}(t)] + [F_r(t)] + [F_{uj}(\theta_A, \dot{\theta}_A, \beta)] \end{aligned} \quad (16)$$

where,  $M = \text{diag}(M_g, M_s)$  is the constant mass and inertia matrix built.  $K_0 = \text{diag}(K_g, K_s)$  is the healthy stiffness matrix (gear subsystem and Cardan shafts subsystem).  $C = \text{diag}(C_g, C_s)$  is the linear viscous damping assembled from the gear subsystem and Cardan shafts subsystem.  $K_{defect} = K_t(\text{pit})$  is the total effective meshing stiffness of a pair of spur gears.

By deriving the global equation of mechanical drive system motion formed of a spur gear subsystem coupled with a Cardan shaft subsystem, as shown in Figure.3, and considering the presence of pits on the tooth surface, the angular displacement of shaft 3 and the lateral displacement of gear and pinion, the governing equations of the global 13-DOF model is formulated as follows in matrices form:

$$\begin{bmatrix}
 m_{y_1} & 0 & 0 & 0 & 0 & 0 & 0 & 0 & 0 & 0 & 0 & 0 & 0 \\
 0 & m_{y_2} & 0 & 0 & 0 & 0 & 0 & 0 & 0 & 0 & 0 & 0 & 0 \\
 0 & 0 & m_{\theta_1} & 0 & 0 & 0 & 0 & 0 & 0 & 0 & 0 & 0 & 0 \\
 0 & 0 & 0 & m_{\theta_2} & 0 & 0 & 0 & 0 & 0 & 0 & 0 & 0 & 0 \\
 0 & 0 & 0 & 0 & m_{\theta_m} & 0 & 0 & 0 & 0 & 0 & 0 & 0 & 0 \\
 0 & 0 & 0 & 0 & 0 & m_{x_3} & 0 & 0 & 0 & 0 & 0 & 0 & 0 \\
 0 & 0 & 0 & 0 & 0 & 0 & m_{y_3} & 0 & 0 & 0 & 0 & 0 & 0 \\
 0 & 0 & 0 & 0 & 0 & 0 & 0 & m_{x_4} & 0 & 0 & 0 & 0 & 0 \\
 0 & 0 & 0 & 0 & 0 & 0 & 0 & 0 & m_{y_4} & 0 & 0 & 0 & 0 \\
 0 & 0 & 0 & 0 & 0 & 0 & 0 & 0 & 0 & m_{\theta_A} & 0 & 0 & 0 \\
 0 & 0 & 0 & 0 & 0 & 0 & 0 & 0 & 0 & 0 & m_{\omega_3} & 0 & 0 \\
 0 & 0 & 0 & 0 & 0 & 0 & 0 & 0 & 0 & 0 & 0 & m_{\omega_4} & 0 \\
 0 & 0 & 0 & 0 & 0 & 0 & 0 & 0 & 0 & 0 & 0 & 0 & m_{\omega_4}
 \end{bmatrix}
 \begin{Bmatrix}
 \ddot{y}_1 \\
 \ddot{y}_2 \\
 \ddot{\theta}_1 \\
 \ddot{\theta}_2 \\
 \ddot{\theta}_m \\
 \ddot{x}_3 \\
 \ddot{y}_3 \\
 \ddot{x}_4 \\
 \ddot{y}_4 \\
 \ddot{\theta}_A \\
 \ddot{\omega}_3 \\
 \ddot{\theta}_B \\
 \ddot{\omega}_4
 \end{Bmatrix}
 +
 \begin{bmatrix}
 c_1 + c_t & -c_t & R_1 c_t & -R_2 c_t & 0 \\
 -c_t & c_2 + c_t & -R_1 c_t & R_2 c_t & 0 \\
 R_1 c_t & -R_1 c_t & R_1^2 c_t + c_p & -R_1 R_2 c_t & 0 \\
 -R_2 c_t & R_2 c_t & -R_1 R_2 c_t & R_2^2 c_t + c_g & 0 \\
 0 & 0 & 0 & 0 & c_p \\
 0 & 0 & 0 & 0 & 0 \\
 0 & 0 & 0 & 0 & 0 \\
 0 & 0 & 0 & 0 & 0 \\
 0 & 0 & 0 & 0 & 0 \\
 0 & 0 & 0 & 0 & 0 \\
 0 & 0 & 0 & 0 & 0 \\
 0 & 0 & 0 & 0 & 0 \\
 0 & 0 & 0 & 0 & 0 \\
 0 & 0 & 0 & 0 & 0
 \end{bmatrix}
 +
 \begin{bmatrix}
 0 & 0 & 0 & 0 & 0 & 0 & 0 & 0 \\
 0 & 0 & 0 & 0 & 0 & 0 & 0 & 0 \\
 0 & 0 & 0 & 0 & 0 & 0 & 0 & 0 \\
 0 & 0 & 0 & 0 & 0 & 0 & 0 & 0 \\
 0 & 0 & 0 & 0 & 0 & 0 & 0 & 0 \\
 c_3 & 0 & 0 & 0 & 0 & 0 & 0 & 0 \\
 0 & c_3 & 0 & 0 & 0 & 0 & 0 & 0 \\
 0 & 0 & c_4 & 0 & 0 & 0 & 0 & 0 \\
 0 & 0 & 0 & c_4 & 0 & 0 & 0 & 0 \\
 0 & 0 & 0 & 0 & c_{\theta_A} + c_g & 0 & 0 & 0 \\
 0 & 0 & 0 & 0 & 0 & c_{\omega_3} & 0 & 0 \\
 0 & 0 & 0 & 0 & 0 & 0 & c_{\theta_B} & 0 \\
 0 & 0 & 0 & 0 & 0 & 0 & 0 & c_{\omega_4}
 \end{bmatrix}
 \begin{Bmatrix}
 \dot{y}_1 \\
 \dot{y}_2 \\
 \dot{\theta}_1 \\
 \dot{\theta}_2 \\
 \dot{\theta}_m \\
 \dot{x}_3 \\
 \dot{y}_3 \\
 \dot{x}_4 \\
 \dot{y}_4 \\
 \dot{\theta}_A \\
 \dot{\omega}_3 \\
 \dot{\theta}_B \\
 \dot{\omega}_4
 \end{Bmatrix}
 +$$

$$\begin{bmatrix} 0 & 0 & 0 & 0 & 0 & 0 & 0 & 0 \\ 0 & 0 & 0 & 0 & 0 & 0 & 0 & 0 \\ 0 & 0 & 0 & 0 & 0 & 0 & 0 & 0 \\ 0 & 0 & 0 & 0 & 0 & 0 & 0 & 0 \\ 0 & 0 & 0 & 0 & 0 & 0 & 0 & 0 \\ 0 & 0 & 0 & 0 & 0 & 0 & 0 & 0 \\ 0 & 0 & 0 & 0 & 0 & 0 & 0 & 0 \\ 0 & 0 & 0 & 0 & 0 & 0 & 0 & 0 \\ 0 & 0 & 0 & 0 & 0 & 0 & 0 & 0 \\ 0 & 0 & 0 & 0 & 0 & 0 & \Gamma_{AB}(\theta_A, \beta) & 0 \\ 0 & 0 & 0 & 0 & 0 & 0 & 0 & 0 \\ 0 & 0 & 0 & 0 & 0 & 0 & 0 & 0 \\ 0 & 0 & 0 & 0 & \Gamma_{BA}(\theta_A, \beta) & 0 & 0 & 0 \end{bmatrix} \begin{bmatrix} \dot{y}_1 \\ \dot{y}_2 \\ \dot{\theta}_1 \\ \dot{\theta}_2 \\ \dot{\theta}_m \\ \dot{X}_3 \\ \dot{Y}_3 \\ \dot{X}_4 \\ \dot{Y}_4 \\ \dot{\theta}_A \\ \dot{\omega}_3 \\ \dot{\theta}_B \\ \dot{\omega}_4 \end{bmatrix} +$$

$$\begin{bmatrix} k_1 + k_{t(pit)} & -k_{t(pit)} & R_1 k_{t(pit)} & -R_2 k_{t(pit)} & 0 \\ -k_{t(pit)} & k_2 + k_{t(pit)} & -R_1 k_{t(pit)} & R_2 k_{t(pit)} & 0 \\ R_1 k_{t(pit)} & -R_1 k_{t(pit)} & R_1^2 k_{t(pit)} + k_p & -R_1 R_2 k_{t(pit)} & 0 \\ -R_2 k_{t(pit)} & R_2 k_{t(pit)} & -R_1 R_2 k_{t(pit)} & R_2^2 k_{t(pit)} + k_g & 0 \\ 0 & 0 & 0 & 0 & k_p \\ 0 & 0 & 0 & 0 & 0 \\ 0 & 0 & 0 & 0 & 0 \\ 0 & 0 & 0 & 0 & 0 \\ 0 & 0 & 0 & 0 & 0 \\ 0 & 0 & 0 & 0 & 0 \\ 0 & 0 & 0 & 0 & 0 \\ 0 & 0 & 0 & 0 & 0 \\ 0 & 0 & 0 & 0 & 0 \end{bmatrix} +$$

$$\begin{bmatrix} 0 & 0 & 0 & 0 & 0 & 0 & 0 & 0 \\ 0 & 0 & 0 & 0 & 0 & 0 & 0 & 0 \\ 0 & 0 & 0 & 0 & 0 & 0 & 0 & 0 \\ 0 & 0 & 0 & 0 & 0 & 0 & 0 & 0 \\ 0 & 0 & 0 & 0 & 0 & 0 & 0 & 0 \\ 0 & 0 & 0 & 0 & 0 & 0 & 0 & 0 \\ k_3 & 0 & 0 & 0 & 0 & 0 & 0 & 0 \\ 0 & k_3 & 0 & 0 & 0 & 0 & 0 & 0 \\ 0 & 0 & k_4 & 0 & 0 & 0 & 0 & 0 \\ 0 & 0 & 0 & k_4 & 0 & 0 & 0 & 0 \\ 0 & 0 & 0 & 0 & k_{\theta_A} + k_g & 0 & 0 & 0 \\ 0 & 0 & 0 & 0 & 0 & k_{\omega_3} & 0 & 0 \\ 0 & 0 & 0 & 0 & 0 & 0 & k_{\theta_B} & 0 \\ 0 & 0 & 0 & 0 & 0 & 0 & 0 & k_{\omega_4} \end{bmatrix} \begin{bmatrix} Y_1 \\ Y_2 \\ \theta_1 \\ \theta_2 \\ \theta_m \\ X_3 \\ Y_3 \\ X_4 \\ Y_4 \\ \theta_A \\ \omega_3 \\ \theta_B \\ \omega_4 \end{bmatrix} = \begin{bmatrix} 0 \\ 0 \\ 0 \\ T_c \\ T_m \\ F_{X_3}(t) \\ F_{Y_3}(t) \\ F_{X_4}(t) \\ F_{Y_4}(t) \\ 0 \\ 0 \\ 0 \\ 0 \end{bmatrix} + \begin{bmatrix} 0 \\ 0 \\ 0 \\ 0 \\ 0 \\ 0 \\ 0 \\ 0 \\ 0 \\ Q_A(\theta_A, \beta) \dot{\theta}_A^2 \\ 0 \\ Q_B(\theta_B, \beta) \dot{\theta}_B^2 \\ 0 \end{bmatrix}$$

Unlike classical models that treat gears and Cardan shafts separately [4-5], this formulation captures the bidirectional coupling between gear mesh excitations and Cardan joint kinematics.

**Table 1.** Basic parameters of spur gear subsystem.

Parameters	Value	
	Driving gear (pinion)	Driven gear (wheel)
Elasticity Module (E) [Pa]	$20.68 \times 10^{10}$	$20.68 \times 10^{10}$
Pressure angle	20°	20°
Poisson's ratio	$3 \times 10^{-1}$	$3 \times 10^{-1}$
Number of teeth pinion and gear	30	90
Pinion ( $R_1$ ) and Gear ( $R_2$ ) base circle radius	30.1 mm	76.1 mm
Pinion mass ( $m_1$ ) and Gear mass ( $m_2$ )	0.96 kg	2.88 kg
Bearing meshing stiffness of pinion ( $k_1$ ) and gear ( $k_2$ )	$65.6 \times 10^6$ N.s/m	$65.6 \times 10^6$ N.s/m
Bearing damping coefficient of pinion ( $c_1$ ) and gear ( $c_2$ )	$18 \times 10^4$ [N.s/m]	$18 \times 10^4$ [N.s/m]
Coupling torsional stiffness of pinion ( $k_p$ ) and gear ( $k_g$ )	$44 \times 10^3$ [N.sm <sup>-1</sup> ]	$44 \times 10^3$ [N.sm <sup>-1</sup> ]
Coupling of damping coefficient of pinion ( $c_p$ ) and gear ( $c_g$ )	$50 \times 10^4$ [Nm.s/rad]	$50 \times 10^4$ [Nm.s/rad]

**Table 2.** Basic Cardan shaft subsystem parameters.

Cardan shaft parameters	Measure and Units	Bearing stiffness	Measure and Units
ShaftsLength of (L)	570 mm	Mesh stiffness ( $k_3=k_4$ )	$7.35 \times 10^5$ Nsm <sup>-1</sup>
Diameter (D) (Shaft 3 = Shaft 4)	75 mm	Bearing damper coefficient( $c_3=c_4$ )	200 Ns/m
Material Density ( $\rho$ )	$7800 \text{ kg/m}^3$	<b>Discs</b>	<b>Measure and Units</b>
Elasticity module (E)	$21.1 \times 10^{10}$ Pa	Mass( $m_A = m_B$ )	$8.45 \times 10^{-1}$ kg
Poisson's ratio	0.3	Eccentricity mass( $m_{a1} = m_{a2}$ )	0.45 g
		Unbalance eccentricity ( $e_1 = e_2$ )	10 mm
		Disc thickness ( $t_{disc}$ )	25 mm

The solution of this system of equations governing the coupled dynamics is carried out using a Runge-Kutta type numerical method, implemented with the ODE45 solver in MATLAB. The duration of each simulation is set to ten seconds. The numerical solution of the model allows us to diagnose the vibration signature of the system. The simulation results are comparatively presented and analysed in the next section, using various signal representations to characterise the impact of the fault.

## 4 Results of Numerical Simulations

The aforementioned equations are used to compare the obtained results from the vibrations of the mechanical drive system operating at a speed of 100 rpm thus of the spur gear subsystem is affected at different severity levels of the pitting (25%).

### 4.1 Numerical Analysis of a Mechanical Drive System

Figures 4 and 5 respectively present the time and frequency representations (by FFT) of the simulated vibration response of shaft 3, in the case of a pitting defect.

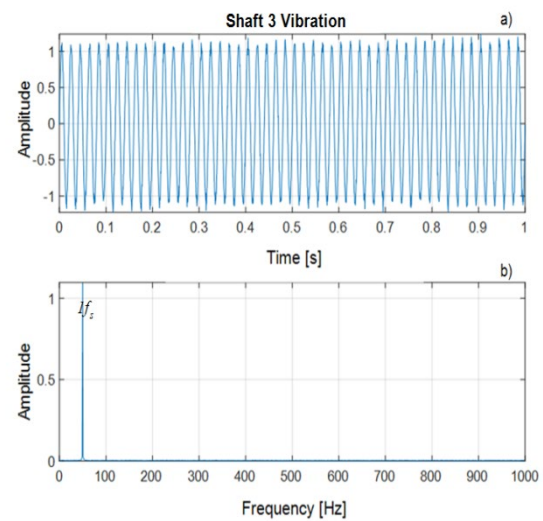


**Fig.4.** Shaft 3 response of a healthy drive system at 100 rpm:(a) Time-domain and (b) FFT.

Figure 4 shows the time response and the corresponding frequency spectrum of the mechanical drive system operating in good condition, without any defects in the spur gear subsystem. In Figure 4(a), the vibration signal shows a stable and quasi-periodic waveform with an almost constant amplitude envelope. This feature reveals a smooth transmission of motion and torque through the gear mesh and shaft 3, without any trace of impulsive events and amplitude modulation. The regular oscillatory pattern reflects the combined effect of the meshing process and the nonhomokinetic excitation inherent in the Cardan joint a phenomenon that remains deterministic and reproducible in the absence of defects. In Figure 4(b), the spectrum is dominated by a single significant spectral component, which corresponds to the fundamental excitation frequency of the drive system. This line can be associated with the primary rotation frequency and the mesh frequency, depending on the measurement point. The absence of significant bands or high-order harmonics confirms that the stiffness of the mesh remains uniform and that no localized defects disturb the contact conditions. Figure 5 shows the response of the system when a pitting defect is introduced into the spur gear. Compared with the

healthy case, noticeable changes are observed in both the time and frequency domains.

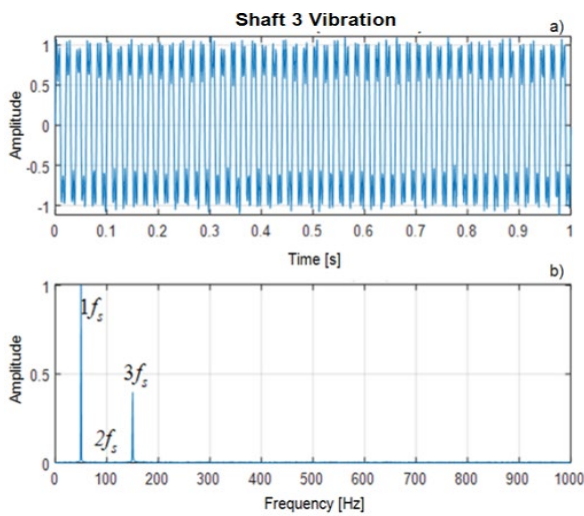


**Fig.5.** Shaft 3 response of a drive system at 100 rpm affected by a pitted gear at 25%: (a) Time-domain and (b) FFT.

In Figure 5(a), the vibration signal shows a clear amplitude modulation, with intermittent high-amplitude fluctuations. These irregularities reflect localized contact disturbances that occur as the pitted tooth area enters and exits the mesh zone. The defect causes a periodic reduction in local mesh stiffness, resulting in transient increases in dynamic force and localized impacts. Consequently, the signal envelope loses its stationarity, reflecting the repeated interaction between the damaged tooth surface and the teeth of the mating gear. In Figure 5(b), the spectrum becomes significantly more complex. In addition to the main mesh frequency, several secondary components and harmonics appear. These components are typically linked to modulation effects caused by the periodic stiffness variation induced by pitting defects. The appearance of bands around the main mesh frequency reveals amplitude and frequency modulation driven by the rotational speed of the gear.

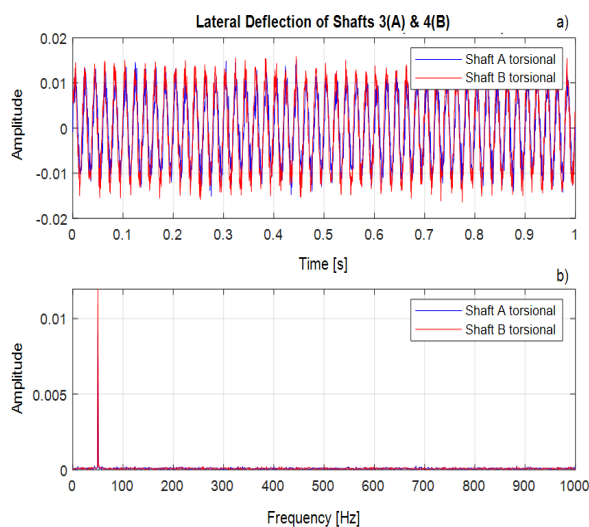


**Fig.6.** Lateral deflection of Cardan Shaft (shafts 3 & 4) of a drive system in good state: (a) and (b).

In Figure 6(a), the lateral deflection response of shafts 3 and 4 shows stable, periodic oscillations of relatively low and limited amplitude. The signals mainly consist of a regular sine waveform, indicating steady-state operation with minimal dynamic disturbances. The close similarity between the responses of shafts 3 and 4 confirms efficient torque transmission and dynamic symmetry at the Cardan joint. In Figure 6(b), the corresponding FFT spectra are characterized by a predominant low-frequency peak with the fundamental shaft rotation frequency. Higher frequency components are negligible, and no significant subharmonics and broadband energy are observed. This spectral signature confirms the absence of transmission-related defects and reflects normal operating conditions with uniform stiffness and load.

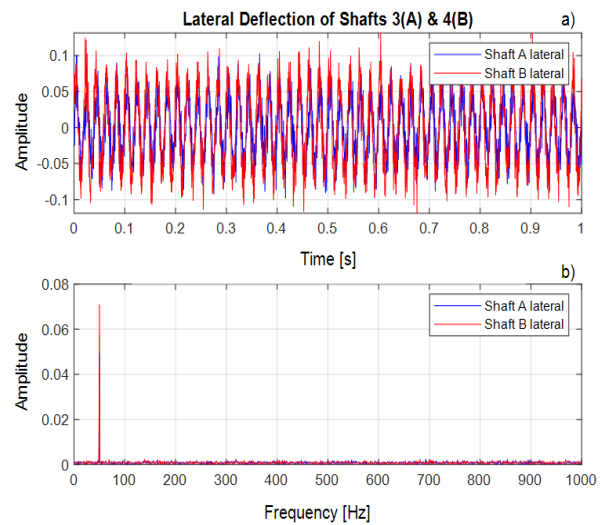


**Fig.7.** Lateral deflection of Cardan Shaft (shafts 3 & 4) of a drive system affect by a pitted gear at 25%: (a) and (b).

In Figure 7(a), the spur gear subsystem is affected by 25% tooth pitting, the lateral deflections of shafts 3 and 4 show a marked increase in the vibration amplitude and a visible modulation of their waveform. The signal becomes less regular, reflecting the presence of time-varying excitation forces propagating along the kinematic chain. This behavior is characteristic of periodic stiffness variations and localized impacts caused by the damaged tooth mesh. In Figure 7(b), the FFT spectra obtained reveals a significant enrichment of the frequency content. In particular, the appearance of additional components and an overall increase in amplitudes compared to the healthy state are observed. Sidebands develop around the dominant rotational frequency, a typical signature of amplitude and frequency modulation induced by a mesh defect. The larger broadband energy, reflects the transfer of fault generated dynamic loads from the gear subsystem to the entire Cardan shaft.

For a subsequent identification and characterisation of the pitting originate from the gear subsystem and transmission error from Cardan shaft subsystem, the steady-state torsional response and its uncontaminated spectral signature provide a solid baseline reference.

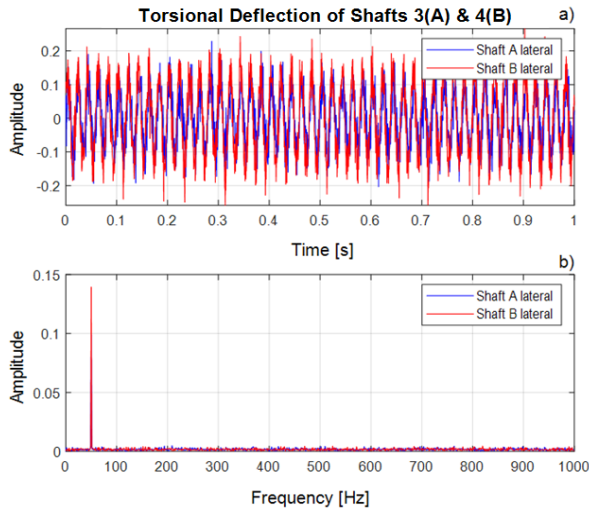


**Fig.8.** Torsional deflection of Cardan Shaft (shafts 3 & 4) of a mechanical drive system in good state: (a) and (b).

In Figure 8(a), the torsional deflection signals of shafts 3 and 4 show stable and periodic oscillations of low and limited amplitude throughout the observation interval. Their waveforms are predominantly sinusoidal and reveal a remarkable similarity between the two shafts. This observation reflects uniform torsional stiffness and efficient torque transmission through the Cardan joint. The absence of abrupt changes, transient peaks, and signal distortion further indicates that the system operates under steady-state conditions with negligible torsion irregularities. In Figure 8(b), it is observed that the FFT spectra of both shafts are dominated by a single low-frequency component, corresponding to the fundamental rotational frequency. Higher-order harmonics and broadband frequency content remain at very low levels, indicating minimal excitation due to nonlinear effects or structural imperfections. The close alignment of spectral amplitudes between shafts 3 and 4 further confirms the dynamic consistency and good mechanical alignment within the entire Cardan shaft.

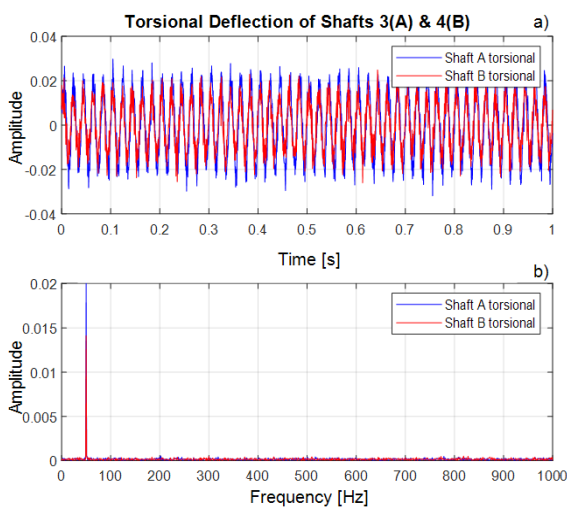


**Fig.9.** Torsional deflection of Cardan Shaft (shafts 3 & 4) of a mechanical drive system with a pitted gear at 25%: (a) and (b).

However, Figure 9 shows the torsional deflection response of the shafts 3 and 4 of the Cardan shaft subsystem when the mechanical drive system is operated with a pitting defect affecting 25% of the tooth surface of the spur gear.

In Figure 9(a), both shafts show oscillatory torsional responses with significant amplitude fluctuations superimposed on them. Compared with defect-free operation, the presence of pitting introduces irregular modulations in the deflection signals of both shafts. These modulations result from periodic perturbations of the transmitted torque, themselves caused by localized reductions in gear mesh stiffness when the degraded tooth area successively makes contact. The effect is transmitted through the gear stage and propagates along the Cardan shaft, causing a torsional response coupled to both the input side (shaft 3) and the output side (shaft 4). The slight difference in amplitude between the two shafts reflects the influence of the joint kinematics and the distribution of inertia within the Cardan joint assembly. In Figure 9(b), a dominant low-frequency component is observed, corresponding to the fundamental rotational frequency of the system. The spectrum also reveals the appearance of secondary components of a relatively low amplitude, absent in the healthy case. These components are related to the modulation effects induced by the pitting defect, where the gear mesh frequency is modulated in amplitude by the shaft rotation frequency. The concentration of spectral energy in the low frequencies indicates that, at this severity level, the defect mainly affects the torque transmission characteristics, without generating high-frequency impulse responses.

#### 4.2 Extraction and Identification of Pitting Fault Features

Orbital deformation provides a clear visual signature of the resulting nonlinear behavior. The thickening and distortion of the trajectory, in contrast to the closed and smooth orbit observed in a healthy state, are sensitive indicators of localized shocks and phase variations induced by the defect.

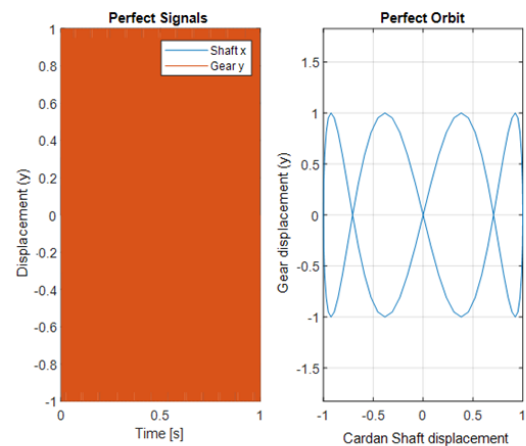


**Fig.10.** Signal and orbit of healthy drive system: (a) and (b). Figure 10 illustrates the healthy operation of the mechanical drive system. In Figure 10(a), the

displacement responses measured on the shaft (x-direction) and spur gear (y-direction) both show stable and periodic waveforms, with amplitudes remaining constant throughout the observation period. This behavior indicates smooth torque transmission and dynamic equilibrium established within the kinematic chain. In Figure 10(b), the corresponding orbital graph (gear displacement as a function of axis displacement) forms a closed, smooth, and regular path. This form is characteristic of synchronous and linear motion between the axle and the gear. The absence of distortion, scattering, and irregular loops indicates that the dynamic coupling effects are limited to the fundamental rotational frequency, confirming the quality of the mesh and the stiffness uniformity throughout the system.

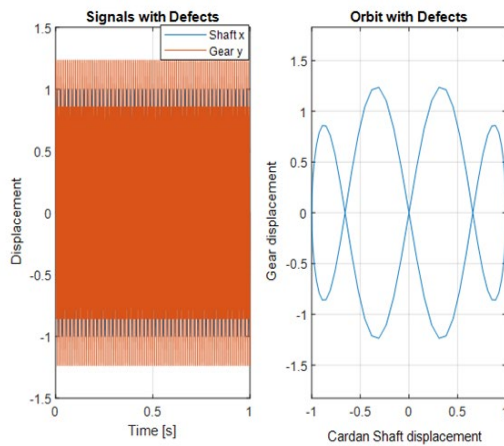


**Fig.11.** Signal and orbit of faulty drive system affected by pitting on teeth surface and transmission error (a) and (b).

Figure 11 illustrates the response of the system when a pitting affects the surface of a spur gear tooth. In Figure 11(a), the gear displacement signal shows a marked increase in high-frequency content and strong amplitude fluctuations compared to the healthy case. These variations reflect localised stiffness changes and intermittent impactions that occur when the damaged tooth is bonded. The axle response, although still periodic, shows increased vibration levels due to the transmission of dynamic forces from the faulty gear through the mechanical coupling. In Figure 11(b), the associated orbital trace becomes distinctly distorted and thickened, moving away from the closed and smooth shape observed under healthy conditions. This orbital spreading reveals amplitude and phase modulation induced by the defect, as well as the presence of additional frequency components related to the mesh frequency and its sidebands. This type of orbital deformation is a characteristic signature of a nonlinear behavior and impulsive excitation, typical of surface damage to the gear teeth.

To complement the analysis and capture the non-stationary nature of the signals, the responses are also analyzed in the time-frequency domain, as presented below.

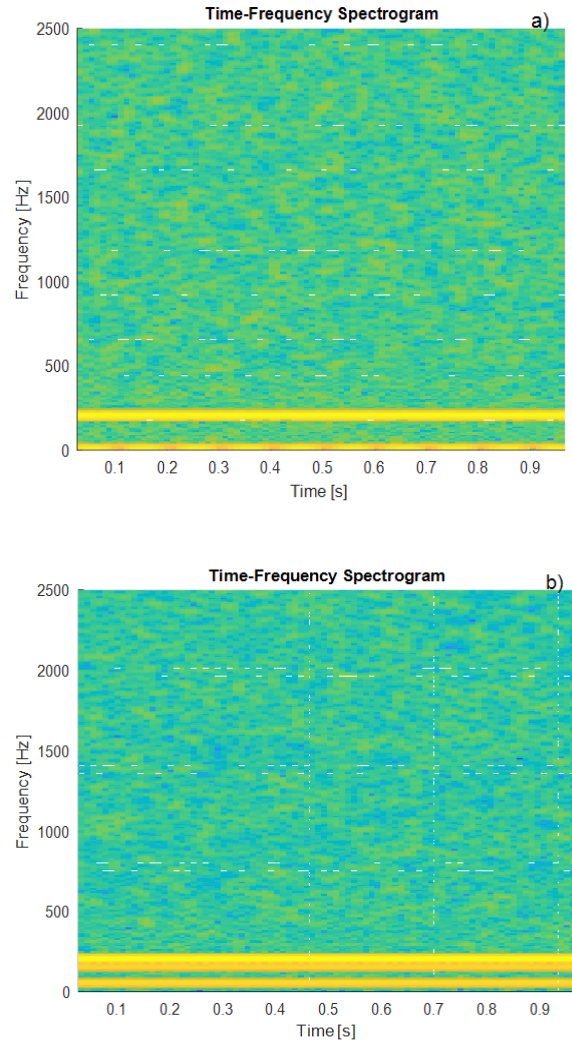


**Fig.12.** Spectrograms of Cardan shaft (shafts 3 &4) of a mechanical drive system: (a) healthy, (b) with a pitted gear at 25%.

Under healthy conditions as show in Figure 12(a), the spectrogram shows a stable and well-organized time-frequency response.

The spectral energy is mainly concentrated in the low-frequency range, corresponding to the fundamental rotational frequency of the drive shaft and its harmonics. These components remain virtually constant over time, indicating smooth torque transmission and nonhomokinetic, but reproducible, joint-induced excitation in the presence of angular misalignment. The absence of significant broadband energy and intermittent high-frequency bursts confirms that the Cardan shaft operates under a uniform dynamic load. When a pitting defect is introduced into the spur gear subsystem, distinct changes appear in the time-frequency response of the drive shaft as shown in Figure 12(b) where the spectrogram reveals an increase in spectral energy density in the low and mid-frequency ranges, accompanied by localized, time-varying intensity fluctuations. These features indicate the presence of amplitude and frequency modulation phenomena, induced by periodic perturbations of the transmitted torque.

Consequently, frequency components appear around the fundamental rotational frequency and its harmonics, producing a spectral response that is less stationary and more diffuse than in the undamaged case. Although no marked high-frequency pulse bands are observed at this level of damage, the progressive spreading of the spectral energy and the emergence of modulated components are characteristic of an early to moderate stage of surface degradation. This confirms that even a relatively moderate pitting defect can influence the dynamic response of the driveshaft, due to the strong coupling between the gear and the Cardan shaft subsystem.

The synthesis of the results and the main implications of this study for fault diagnosis are discussed in the final section, which also presents the main conclusions and research perspectives.

## 5 Discussion

In depth analysis of the simulation results validates the ability of the 13-DOF coupled dynamic model to capture the influence of a pitting defect on the vibration response of a mechanical drive system incorporating a Cardan shaft subsystem and spur gear subsystem. Systematic comparison between healthy and defective states reveals several robust diagnostic signatures.

First, the impact of the defect manifests as a stationarity disturbance in the time domain. The amplitude modulations and irregular fluctuations observed in the lateral and torsional deflections are a direct consequence of the periodic and localised reduction in mesh stiffness when the pitted tooth is attached. This phenomenon is clearly attributed to the defect, distinct from the natural nonhomokinetic excitation of the cardant joint.

Second, in the frequency domain, the defect induces a characteristic spectral enrichment. The appearance of secondary components and, above all, sidebands around the fundamental rotation frequency and the mesh frequency, constitute a classical signature of amplitude and frequency modulation. This signature is directly correlated with the cyclic variation of stiffness due to pitting.

Third, time-frequency analysis (spectrogram) allows visualization of the temporal evolution of these modulations. The defective response is distinguished by an increase in energy density and localised fluctuations, contrasting with the stable of the healthy case. This representation confirms that the defect introduces nonstationarity into the dynamic response.

Finally, the deformation of the orbits provides a powerful visual signature of the induced nonlinear behavior. The coarsening and distortion of the trajectory, compared to the closed and smooth orbit of the healthy state, are sensitive indicators of the localised shocks and phase variations caused by the defect.

These observations converge to demonstrate the existence of a strong dynamic coupling between the gear subsystem and the entire Cardan shaft subsystem. The disturbances generated at the pitted tooth propagate efficiently through the kinematic chain, affecting the overall response. The reference response of the healthy

system, characterised by its stability and spectral purity, thus establishes an essential basis for the early identification of defects.

## 6 Conclusion

This study developed and validated a torsionally-laterally coupled dynamic model of 13 degrees of freedom for a realistic mechanical drive system combining a spur gear and misaligned Cardan shaft. The model uniquely incorporates the effect of progressive pitting defects through an explicit modeling of their impact on the transmission shaft (Cardan shaft). Numerical simulations identified characteristic vibration signatures of pitting, even at a moderate stage (25% of the affected surface area). The main indicators identified are:

- Amplitude modulations and loss of stationarity in the time-domain signals.
- The appearance of sidebands and an enrichment of the frequency spectrum.
- A diffuse time-frequency structure with localized energy fluctuations.
- Significant orbital deformation, indicative of nonlinear excitations.

These results highlight the need to consider dynamic couplings in the modeling of complex transmissions for accurate diagnosis. They validate the proposed unified modeling approach as an effective tool for understanding fault propagation and developing predictive maintenance strategies based on advanced vibration analysis.

Future work could include experimental validation of the model, extending the analysis to more severe or multiple failures, and exploring advanced signal processing techniques for automated extraction of identified fault features.

**Acknowledgments:** The authors are grateful for the resources and equipment provided by the Department of Industrial Engineering, Operation Management, and Mechanical Engineering at Vaal University of Technology (South Africa) to enable this work.

**Fundings:** No available.

**Data availability statement:** The authors attest to the utmost integrity in the recording, processing and reporting data.

**Author Contributions:** Y.H.K.H.: conceptualization, methodology, software, validation, formal analysis, data curation original draft, writing review and editing; B.X.T.K.: review, and editing original draft and supervision; A.A.A.: review and editing.

## References

1. F. Chaari, W. Baccar, M. Haddar, N. Tandon, Dynamic response simulation of a spur gear system with localized tooth defects. *Journal of Mechanical Design*, 128(2), 338–348 (2006).

2. R.B. Randall, *Vibration-based Condition Monitoring: Industrial, Aerospace and Automotive Applications*. John Wiley & Sons (2011).
3. H. Ma, J. Zeng, R. Feng, X. Pang, B. Wen, An improved dynamic model for gear systems with tooth surface wear. *Mechanical Systems and Signal Processing*, 60–61, 538–553 (2015).
4. B.X. Tchomeni, and A. A. Alugongo. "Experimental analysis of a cracked cardan shaft system under the influence of viscous hydrodynamic forces." *Fluids* 8.7 (2023): 211.
5. K.M. Al-Hussain, Dynamic stability of two shafts connected through a universal joint. *Journal of Sound and Vibration*, 266(1), 1–18 (2003).
6. Z.K. Peng, F.L. Chu, Application of the wavelet transform in machine condition monitoring and fault diagnostics. *Mechanical Systems and Signal Processing*, 18(2), 199–221 (2004).
7. J. Wang, I. Howard, Finite element analysis of high contact ratio spur gears in mesh. *Mechanical Systems and Signal Processing*, 19(2), 263–287 (2005).
8. A. Kahraman, R. Singh, Interactions between time-varying mesh stiffness and clearance non-linearities in a geared system. *Journal of Sound and Vibration*, 146(1), 135–156 (1991).
9. A. Parey, N. Tandon, Spur gear dynamic models including defects: A review. *Shock and Vibration Digest*, 35(6), 465–478 (2003).
10. G. Genta, *Dynamics of Rotating Systems*. Springer, New York (2007).